Feedlot is a unique and constant source of atmospheric ice-nucleating particles

Naruki Hiranuma[1], Brent W. Auvermann[2], Franco Belosi[3], Jack Bush[2], Kimberly M. Cory[1,4], Romy Fösig[5], Dimitri Georgakopoulos[6], Kristina Höhler[5], Yidi Hou[1], Harald Saathoff[5], Gianni Santachiara[3], Xiaoli Shen[5,7],
5   Isabelle Steinke[5,8], Nsikanabasi Umo[5], Hemanth S. K. Vepuri[1], Franziska Vogel[5], Ottmar Möhler[5]

[1]Department of Life, Earth, and Environemntal Sciences, West Texas A&M University, Canyon, TX 79016, USA
[2]Texas A&M AgriLife Research, Amarillo, TX 79106, USA
[3]Institute of Atmospheric Sciences and Climate, National Research Council, Bologna, 40129, Italy
10   [4]Department of Environmental Toxicology, Texas Tech University, Lubbock, TX 79409, USA
[5]Institute of Meteorology and Climate Research, Karlsruhe Institute of Technology, Karlsruhe, 76021, Germany
[6]Department of Crop Science, Agricultural University of Athens, Athens, 118 55, Greece
[7]Department of Earth Atmospheric and Planetary Sciences, Purdue University, West Lafayette, IN 47907, USA
[8]Atmospheric Sciences & Global Change, Pacific Northwest National Laboratory, Richland, WA 99354, USA

Correspondence: Naruki Hiranuma (nhiranuma@wtamu.edu)

Keywords. ice, freezing, cloud, feedlot

20   **Abstract.** This study presents a comprehensive investigation of ice-nucleating particles (INPs) in the surface materials and aerosol particles from U.S. cattle feeding facilities. Using a modern suite of online and offline aerosol particle characterization instruments, we conducted a three-year field survey (2016-2019), Aerosol Interaction and Dynamics in the Atmosphere (AIDA) cloud chamber experiments, and ice crystal residual (ICR) analyses for the feedlot sample. Our results showed unique supermicron size dominance in the feedlot INPs with a high concentration of INPs (several hundred and thousand INPs L^{-1} at -20°C and -25°C, respectively).
25   Thus, agricultural fields, especially animal feeding facilities, represent important INP sources if these particles rise to sufficient height in the atmosphere. New data on the ice nucleation (IN) properties of agricultural dust at heterogeneous freezing temperatures (Ts > -29°C) were generated, providing statistical context. Overall, we successfully characterized physical, chemical, and biological properties of aerosol particles found at a cattle feedlot, thereby finding their unique heat-tolerant nature. The relationship between these measured properties and atmospheric IN parameterization relevant to mixed-phase clouds is discussed. Our INP
30   parameterization and ICR characterization are meaningful for improved understanding of INP emission and cloud microphysical processes in the supermicron-particle laden region. These unique INPs may directly influence the lifetime of supercooled clouds in a unique manner for this region. An application of our IN parameterization is crucial to explore INP relations to supercooled cloud properties over such a predominant agricultural area.

1. Introduction

35

1.1. Overview. Agricultural land use is in excess of 50% of total U.S. land use according to U.S. Department of Agriculture, and there are > 26,000 feedlots in the U.S. (Drouillard, 2018). Globally, agricultural practices represent a substantial dust emission source, accounting for up to 25% of total (Ginoux et al., 2012), and may in part contribute to recent climate change and hydrological cycle alternation in the U.S. (Overpeck and Udall, 2020). In particular, the Texas Panhandle is a major contributor to U.S. cattle
40   production, accounting for 42% of fed beef cattle in the U.S. and 30% of the total cattle population in Texas (> 11 million head), annually producing > 5 million tons of manure on an as-collected basis according to Texas A&M AgriLife Research. Agricultural dust particles observed at animal feeding operations have long been known to affect regional air quality in the Texas Panhandle (Von Essen and Auvermann, 2005). Specifically, open-air feedlots (OAFs) in proximity to West Texas A&M University represent a significant emission source of dust particles, dominated by supermicron sizes in volume equivalent diameter (D_{ve}), resulting in a
45   24-hour averaged OAF dust concentration as high as 1200 μg m^{-3} (Hiranuma et al., 2011). The emission flux of PM$_{10}$ (i.e., particulate matter smaller than 10 μm in diameter) from OAFs in this region exceeds 4.5 μg m^{-2} s^{-1} up to 23.5 μg m^{-2} s^{-1} depending on stocking density (Bush et al., 2014). Interestingly, our previous study revealed an inclusion of OAF-derived particles at 3.5 kilometers downwind of the feedlot, suggesting their regional scale impact (Hiranuma et al., 2011). Moreover, some recent studies suggest that aerosol particles emitted from agricultural activities might reach out to cloud heights due to wind erosion and other
50   relevant mechanisms (Steinke et al., 2020 and references therein; Katra, 2020; Duniway et al., 2019). However, their impact in cloud microphysics, especially IN, is overlooked and poorly constrained, although this region in the U.S. Southern High Plains is dominated by deep convective clouds, where aerosol-cloud interactions, including cloud microphysics of INPs, play a crucial role in precipitation and thunderstorm processes (Li et al., 2017). To fill this gap, we comprehensively researched immersion mode freezing abilities (i.e., the freezing propensity of INP immersed in supercooled water; see Vali et al., 2015) and other important
55   properties, including physical, chemical, and biological properties, of feedlot surface materials sampled at commercial and research OAFs in Texas. Recent modeling simulation and remote sensing studies suggest that immersion freezing, focused in this study, is

the most relevant heterogeneous IN mechanism (out of several) through which ice crystals are formed in mixed-phase clouds (Hande and Hoose, 2017; Westbrook and Illingworth, 2011).

1.2. Objective. Our specific objective was to answer the following research questions: *[1] How do ambient INP results compare to samples of feedlot surface materials? What are the INP fractions of segregated supermicrometer OAF particles?* In this study, we compared IN ability of ambient OAF dust (sampled in the field and analyzed in the offline lab setting) to surface material samples aerosolized in the cloud simulation chamber to shed light on long-standing discussion regarding the representativeness of dried, pulverized surface materials as surrogates for ambient dust particles in immersion freezing tests (Boose et al., 2016). *[2] What are the contributions of OAF particle composition to INP propensity?* OAF-emitted particles are known to include organic materials. Our previous work using Raman micro-spectroscopy revealed that ambient dust sampled at OAFs is composed of brown or black carbon, hydrophobic humic acid, water soluble organics, less soluble fatty acids and those carbonaceous materials mixed with salts and minerals (Hiranuma *et al.*, 2011). Recently, organic acids (i.e., long-chain fatty acids) and heat stable organics were found to be acting as an efficient INP (DeMott et al., 2018; Perkins et al., 2020). However, our knowledge regarding what particulate features of OAF dust trigger immersion freezing in heterogeneous freezing Ts (i.e., size vs. composition) is still lacking. To improve our knowledge, we conducted single particle composition analyses of different types of OAF ICR samples. *[3] Can we identify any biological INPs? How does heating influence INP abundance in samples of feedlot surface materials?* On average, a beef animal produces 82 lb. per day (wet or as-is basis) of manure that is a complex microbial habitat, containing bacteria and other microorganisms, and is the predominant source of OAF dust when dried (Von Essen and Auvermann, 2005). For instance, the cattle manure hosts a wide variety of bovine rumen bacteria (i.e., *Prevotellaceae*, *Clostridiales*, lipoprotein components of certain bacterial cell walls) as well as non-bacterial fauna of the rumen, such as fungal spores, lichens, fungi, *Plantae*, *Protista*, *Protozoa*, *Chromalveolata,* and *Archaea* (Nagaraja, 2016). In this study, we examined if any IN active cattle bovine microorganisms could be identified when aerosolized. Further, biogenic aerosol particles were found to promote nucleation of ice (Després et al., 2012; Suski et al., 2018), and they may be identified by comparing the IN ability of heat-treated samples to non-heat-treated samples. The heat tolerance of supermicron dominant INPs in a test proxy dust (i.e., Arizona Test Dust, A2 fine test dust, Powder Technology Inc.) was previously found (Perkins et al., 2020). Our study complements this previous study by examining the heat tolerance of 'natural' organic-rich surface material samples.

2. Materials and Methods

2.1. Ambient samples. Aerosol particles were collected at OAFs to assess immersion freezing properties of "ambient" OAF samples. These field samples were collected using 47 mm Nuclepore filters (Whatman, Track-Etched Membranes, 0.2 um pore). A filter holder was deployed at ~1.5 m above the ground. The filter sampling conditions measured locally (during individual sampling activities) are summarized in **Table 1**. We sampled OAF particles in a wide variety of seasons and conditions, conducting ambient aerosol particle samplings at the downwind edge of four different commercial feedyard (FY) facilities (> 45,000 head capacity, anonymously denoted as FY I-IV) within a 33-mile radius of West Texas A&M University using an identical sampler in 2017–2019. To complement our downwind measurements, we conducted the sampling at the upwind side at FY I in 2017 to check the field background INPs. Our sampling durations varied, but were up to ~4.5 hours, and our final IN efficiency results were scaled to the sampled volume of air afterwards. All filter samples were kept in sterilized tubes refrigerated at 4°C until the immersion freezing measurements, addressed in **Sect. 2.5**, began (typically within 24 hours after sampling).

2.2. Surface samples. Besides field samples, we used two different types of OAF surface materials, namely TXD01 and TXD05, as surrogates for dust particles observed at the downwind location of OAFs in Texas. These proxy samples were used in our controlled lab study at the AIDA facility. TXD01 is a composite sample of surface soils from several commercial and experimental cattle feedlots located in West Texas. The other sample (TXD05) originates from a research feedlot in McGregor, TX. Both samples represent a raw surface material composite from feedlot pens, where cattle are fed without antibiotics or probiotics. All samples were ground, hammer-milled, and sieved for < 75 μm in grain size. Moreover, dry-heated samples (i.e., 100°C oven-dried for approximately 12 hours) of each type were examined in this study to assess the heat tolerance of TXD INPs. In addition, wet-boiled samples (i.e., filter samples suspended in pure water and boiled for 20 minutes) were also examined using an offline freezing technique. Each sample was injected into the AIDA chamber using a rotating brush disperser (PALAS, RGB1000) followed by passing through a series of inertial cyclone impactor stages to be sure to limit particle size of < 10 μm in D_{ve}. Subsequently, the OAF particle size distribution in the AIDA chamber was measured prior to each simulated adiabatic expansion experiment.

A summary of our sample physical properties is provided in **Table 2**. Briefly, bulk density values of all samples were measured using a gas displacement pychnometer (Quantachrome, 1200e Ultrapyc). As seen, all measured densities are almost identical, or there is at least no systematic difference between non-heated material densities and pre-heated ones, which may be indicative of heat-resistant features potentially due to pre-exposure to soil T on average higher than ambient T even at the depth of 150 mm during summer (Cole et al., 2009). Next, geometric specific surface area (*SSA*) values were computed based on AIDA aerosol particle size distribution measurements (i.e., fraction of total surface area concentration to total mass concentration estimated from our size distribution data; see **Table 3**). Another measurement of nitrogen adsorption-based *SSA*, Brunauer-Emmett-Teller (BET) *SSA*, for each system are also shown in **Table 2**. The measured BET *SSA* values of OAF samples are slightly

higher compared to those of previously measured agricultural soil dust samples (0.74–2.31 m^2 g^{-1}) (O'Sullivan et al., 2014), but similar to that of microcline (K-feldspar; 3.2 m^2 g^{-1}) (Atkinson et al., 2013) that is known to contain surfaces with a substantial amount of porous structures (Kiselev et al., 2017). On average, our geometric *SSA* value (± standard error) is 4.59 ± 0.81 m^2 g^{-1}, which is higher than the BET *SSA* values. As demonstrated in our previous studies, a small *SSA* value generally indicates the

5   presence of a large aerosol particle population (Hiranuma et al., 2015). Hence, the predominance of large bulk powders assessed in BET is presumably responsible for the observed differences in these two *SSA* values (**Table 2**). Indeed, the particles observed in AIDA were all < 6.5 μm D_{ve} (**Table 3**), whereas the particles evaluated by BET were up to 75 μm. Therefore, in association with large grain size involved in the BET analysis, bulk samples might have exhibited smaller *SSA* than dry dispersed ones. Furthermore, our *SSA* measurements suggest heat-tolerance in our OAF samples. We examined BET *SSAs* using two different degassing *T*s

10   (55°C and 200°C) for each sample, and we did not observe any deviations exceeding 10% accuracy. Geometric *SSAs* of non-heated and heated samples also agreed within given standard errors.

2.3. Instrumentation overview. We used the AIDA-controlled expansion cloud-simulation chamber (Möhler et al., 2003) and an array of analytical instruments at Karlsruhe Institute of Technology to investigate the ice-nucleating properties, in particular

15   immersion freezing (Vali et al., 2015), and to characterize other properties of OAF particles. More specifically, DNA sampling for metagenomics analysis was also conducted to study biological components of the OAF bulk/aerosolized samples. Complementary filter sampling of the aerosol particles directly from the AIDA chamber was performed prior to expansion experiments, and these samples were used to examine INPs in the dynamic filter processing chamber (DFPC) (Santachiara et al., 2010). The DFPC technique was used to measure the number concentration, ice-activation fractions, and the nucleation site density of the INPs under

20   different *T* conditions and for different particle sizes (i.e., PM$_1$ vs Total). To complement the AIDA chamber immersion results, the IN SpEctrometer of the Karlsruhe Institute of Technology (INSEKT) was used for filter samples as well as < 75 μm sieved-bulk samples collected (Schiebel, 2017).

Another motivation for using the AIDA facility is its ice-selecting pumped counterflow virtual impactor (IS-PCVI). The IS-PCVI instrument separates ICRs from interstitial particles, including cloud droplets (Hiranuma et al., 2016). Preserving ICRs,

25   which are leftover INPs after the evaporation of water content, by the IS-PCVI is key for elucidating physicochemical identities of INPs. ICRs were collected using TEM-grids (Ted Pella Inc., 01844N-F/01896N-F/162-100), and also compared to the total aerosol particles collected directly from the AIDA chamber on Nuclepore™ filters (Whatman, Track-Etched Membranes, 0.2 um pore). More detailed information of our IS-PCVI experiments in this study is provided below. Offline single particle analyses were conducted using an electron microscope (JEOL, JSM-6010LA) equipped with an energy dispersive X-ray spectroscopy function.

30   Through this unique capability and subsequent analyses of ICR samples, we obtained detailed information on ICR composition of individual particles. In addition, we used a single particle mass spectrometer to characterize aerosol particle chemical compositions of our surface samples presented in **Supplemental Information (SI) Sect. S1**. Individual details of all lab and field instruments and techniques are introduced in **Sects. 2.4 – 2.8**.

35   **2.4. AIDA platform and IN experiments.** We chose the AIDA chamber as our study platform because using this chamber is appropriate for studying ice formation in mixed-phase clouds in a controlled setting with respect to both *T* and saturation (Möhler et al., 2003). This chamber generates artificial clouds and activates particles in a simulated atmospheric cloud parcel via expansion cooling. The air volume adjacent to the chamber wall in the 84 m^3 vessel is much smaller in comparison to the actively mixed volume of the vessel. Hence, we neglect the wall effect (e.g., particle wall deposition) in the AIDA experiment. The AIDA has

40   been applied for the analysis of both ambient and lab-generated INPs and has facilitated characterization of many INP species (Hoose and Möhler, 2012). Note that the AIDA results provided a validation of the other INP spectrometers employed in this study.

Prior to each expansion experiment, a combination of a scanning mobility particle sizer (TSI Inc., Model 3080 differential mobility analyzer and Model 3010 condensation particle counter), an aerosol particle sizer (TSI Inc., Model 3321), and a counter (CPC; TSI Inc., Model 3076) collectively measured the total number and size distribution of aerosol particles at the horizontally

45   extended outlet of the AIDA chamber. Followed by the injection and size distribution measurement, each sample was examined for its immersion freezing ability by the expansion experiment individually.

As shown in **Table 3**, we conducted 10 AIDA experiments. All lab data associated with this study were archived according to the AIDA experiment number. As seen in **Table 3**, the mode diameters of TXD01 samples in AIDA were in general smaller than TXD05 samples, consistent with our *SSA* measurements (see **Table 2**). Shown in **Fig. 1** are expansion experiment profiles of

50   these 10 experiments with different samples, including TXD01 (i)–(iii), TXD05 (iv)–(vi), TXD01H (vii–viii), and TXD05H (ix–x). These profiles represent data points measured in the chamber over a series of time, such as *T* (a), pressure (b), relative humidity (*RH*, c), and aerosol particles and hydrometeor concentration (d) for each AIDA experiment. The pressure within the chamber was reduced (Δ*P* ≈ 180 - 290 hPa), causing the *T* to drop and a simulated adiabatic 'expansion' to occur. As can be seen, measurements were made by AIDA-simulated immersion freezing at water saturation (*RH* with respect to water around 100%). A droplet-ice

55   threshold typically coincides with ≥ 20 μm D_{ve} (Hiranuma et al., 2016). Thus, the number concentration of > 20 μm D_{ve} AIDA particles measured by a welas optical particle counter (Benz et al., 2005) primarily represents pristine ice crystals formed during the expansion (**Figs. 1d**).

2.5. Offline immersion freezing experiment techniques. To assess the ambient INP concentration through samples collected in the field, we used an offline droplet-freezing assay instrument, the West Texas Cryogenic Refrigerator Applied to Freezing Test system (WT-CRAFT) (Hiranuma et al., 2019; Cory, 2019). Briefly, WT-CRAFT enables a simulation of atmospheric immersion freezing using aerosol particles containing supercooled droplets at T > -25°C. WT-CRAFT was a replica of NIPR-CRAFT (Tobo, 2016), but the two systems currently possess different sensitivities to artifact and detectable T ranges as described in Hiranuma et al. (2019). In this study, we evaluated 70 solution droplets (3 μL each) placed on a hydrophobic Vaseline layer per experiment at a cooling rate of 1°C min^{-1}. All droplets were prepared using filter rinse suspensions with HPLC-grade water. The amount of HPLC water was determined based on the total amount of air sampled through the cross section of filter (**Table 1**) with a detection capability of 0.001 INP per L (standard T and pressure, STP) of air. In other words, the first frozen droplet observed was considered as 0.001 INP L^{-1} in this study. The freezing moment was determined optically based on the change in droplet brightness when the initially transparent liquid droplets became opaque upon freezing. If the freezing temperature (T) was not obvious for any droplets, the 8-bit grayscale images were assessed using ImageJ software to determine the T of phase shift. After the measurement, we calculated the frozen fraction and estimated the INP concentration per volume of air as a function of T for every 0.5°C following the parameterization described in Eqns. 1-2 of DeMott et al. (2017). As shown in Hiranuma et al. (2019, i.e., Table S2), the T uncertainty in WT-CRAFT is ± 0.5°C. The n_{INP} uncertainty is typically represented by 95% binomial confidence internal (CI95%).

The INSEKT system is another offline immersion freezing technique used to assess TXD samples collected on 47 mm polycarbonate filter (0.2 μm pore size) at the AIDA facility. All filter samples were collected with a sampling flow rate of 10 L min^{-1}, and a total of ≈600 L of air was sampled through a cross section of each filter (see **Table 3** for corresponding AIDA experiments). As described in Schiebel (2017), a design and concept of INSEKT is based on the CSU-IS instrument (Hill et al., 2014 and 2016). With 96 wells (50 μL suspension to fill for each), INSEKT estimated reasonable INP concentrations per unit volume of suspension as well as air along with binomial CI95% for each sample according to Eqns. 3.18 – 3.21 in Schiebel (2017). In this study, filter-collected aerosol particles were suspended in 8 ml filtered nanopure water, that has negligible contribution to background freezing, and used for characterizing their IN efficiency (Schneider et al., 2020). Similar to WT-CRAFT, the amount of pure water to generate a stock suspension was adjusted for the first frozen aliquot-well observed to be considered as ≈0.015 INP L^{-1} in this study based on the total amount of air sampled through the cross section of filter. A series of diluted suspensions (x15 and x225) was consistently analyzed for each sample to acquire an INP spectra covering a wide range of heterogeneous freezing temperatures (-7.5 ºC to -25.5 ºC). For the overlapping temperatures, we chose the data exhibiting the minimum CI as representative n_{INP} for given T. In addition, **SI Sect. S2** provides a comparison of our two immersion freezing techniques, which are reasonably correlated.

Immersion/condensation mode INP concentrations were also measured at CNR-ISAC by means of the Dynamic Filter Processing Chamber (DFPC) (Santachiara et al., 2010; Hiranuma et al., 2019). The DFPC chamber is a replica of the Langer dynamic developing chamber (Langer and Rogers, 1975). A systematic uncertainty in terms of T in DFPC is within ± 0.1°C (Table S1 in Hiranuma et al., 2019). With a water saturation error of ± 0.01, an ice detection error of ± 33%, and the experimental standard deviation, the overall $n_{s,geo}(T)$ uncertainties of DFPC are estimated to be ± < 62% for this study. The application of DFPC for immersion freezing has been verified in previous inter-comparison studies (DeMott et al., 2018; Hiranuma et al., 2019). For the DFPC analyses, aerosol particles were collected on nitrocellulose black gridded membrane filters (0.45 μm porosity Millipore) from the AIDA chamber prior to each expansion experiment (**Table 3**). Two parallel samplers employed in this study had an identical sampling flow rate of 2 L min^{-1}, and a total of 100 L of air was sampled for each system. One sampling system collected the total aerosol particles, while another one was equipped with a cyclone impactor (MesaLabs, SCC0732, S/N 13864) to collect only submicron-sized aerosol particles. This impactor is characterized with a cut-off size around 1 μm in aerodynamic diameter (50% cut-off diameter at 0.9 μm) at 2 L min^{-1} flow rate (Kenny, et al., 2000). Therefore, the latter line selectively collected particles smaller than 1 μm in diameter. The cut-size efficiency of this cyclone impactor was tested in the lab against NaCl particles. Particle transmission efficiency along the total sampling line was taken into account by estimating gravitational losses in the horizontal tract of the sampling tube and inertial losses in the bend. At particle size of 10 μm (larger than what was measured in the AIDA chamber), the overall particle transmission efficiency was higher than 86%. For a particle size of 2 μm, the particle loss is estimated to be ≈2.5%. Due to the small loss, we neglected any corrections for aerosol particle counts. After collection, the filters were safely kept in Petri dishes at room T until the freezing experiments were initiated.

2.6. Extraction of total DNA from bulk and aerosolized dust samples. Total DNA was extracted from Texas dust samples TXD01 and TXD05 prior to and after aerosolization in the AIDA cloud chamber. From bulk samples of dust, total DNA was extracted from 157.1 mg (TXD01) and 128.8 mg (TXD05). To sample aerosolized dust from the AIDA cloud chambers, steel filter holders containing nucleopore filters (47mm diameter and 0.2 μm pore size) were used. These filters were previously sterilized in a standard vapor autoclave and fitted onto the AIDA cloud chamber for aerosol particle sampling prior to the expansion IN experiment. After the conclusion of the experiments, the holders were removed from the chamber to extract total DNA directly from the nucleopore filters. DNA extractions were performed using the FastDNA® Spin Kit for Soil (MP Biomedicals) as described in the manufacturer's protocol. Filters were aseptically removed from holders and placed in the Lysing Matrix E tube for mechanical cell disruption, which was carried out with the FastPrep® Instrument (MP Biomedicals). The concentration and purity of the extracted DNA was measured by using the Qubit™ 3.0 (Thermo Fisher Scientific). The volume of each sample was 50-100 μL.

Next, our metagenomics analysis method of total DNA is described. The amplification of phylogenetic marker genes and the metagenomics analysis of amplicons from each dust sample were performed by Eurofins Genomics Germany GmbH using the INVIEW Microbiome Profiling 3.0 protocol in order to identify and classify the microbial population (*Fungi*, *Bacteria*, and *Archaea*) of each sample. To achieve this, the hypervariable regions V1-V3 and V3-V5 of the bacterial 16SrRNA gene, the fungal
5   internal transcribed spacer (ITS2) gene and part of the archaeal 16SrRNA gene were amplified by polymerase chain reaction from each sample using in-house primers. Amplicons were sequenced with the MiSeq next generation sequencing system with the 2x300 bp paired-end read module.

As the first step of the microbiome analysis, all reads with ambiguous bases ("N") were removed. Chimeric reads were identified and removed based on the de-novo algorithm of UCHIME (Edgar et al., 2011) as implemented in the VSEARCH package
10   (Rognes et al., 2016). The remaining set of high-quality reads was processed using minimum entropy decomposition (MED) (Eren et al., 2013 and 2015). MED provides a computationally efficient means to partition marker gene datasets into operational taxonomic units (OTUs). Each OTU represents a distinct cluster with significant sequence divergent from any other cluster. By employing Shannon entropy, MED uses only the information-rich nucleotide positions across reads and iteratively partitions large datasets while omitting stochastic variation. The MED procedure outperforms classical identity-based clustering algorithms.
15   Sequences can be partitioned based on relevant single nucleotide differences without being susceptible to random sequencing errors. This allows a decomposition of sequence datasets with a single nucleotide resolution. Furthermore, the MED procedure identifies and filters random "noise" in the dataset, i.e., sequences with very low abundance (less than 0.02% of the average sample size).

To assign taxonomic information to each OTU, DC-MEGABLAST alignments of cluster-representative sequences to the
20   sequence database were performed. The most specific taxonomic assignment for each OTU was then transferred from the set of best-matching reference sequences (lowest common taxonomic unit of all the best matches). A sequence identity of 70% across at least 80% of the representative sequence was the minimal requirement for considering reference sequences. Further processing of OTUs and taxonomic assignments was performed using the QIIME software package (version 1.9.1, http://qiime.org/). Abundances of bacterial taxonomic units were normalized using lineage-specific copy numbers of the relevant marker genes to
25   improve estimates (Angly, 2014). Taxonomic assignments were performed using the NCBI_nt reference database (Release 2019-01-05).

2.7. Ice-selecting pumped counterflow virtual impactor (IS-PCVI) sampling. The IS-PCVI is a custom-built instrument that can accommodate a substantially larger counterflow in comparison to commercially available PCVIs (e.g., Boulter et al., 2006).
30   Such a large counterflow allows the IS-PCVI to have critical cut-off sizes of larger than 10 μm (more than twice as large as regular PCVIs) and, therefore, to inertially separate ice crystals from droplets found in mixed-phase clouds. As described in Hiranuma et al. (2016), the development of the IS-PCVI was guided by computation fluid dynamics simulations, and performance was verified in the lab using the AIDA chamber. Verifications include its transmission efficiencies and cut-sizes up to ~30 μm, ice phase separation based on the cut-size, validation of the evaporation section as part of the IS-PCVI outlet, performance of the interstitial
35   particle sampling and minimum artifact detection (up to 5%).

IS-PCVI properties were determined to realize the critical cut-size of ice crystals >24 micron diameter estimated based on Fig. 9 of Hiranuma et al. (2016). During TXDUST01, the output flow was fixed at 2.5 lpm. Contrarily, the input and counter flows were slightly varied as listed in the table. Nonetheless, we used a moderate virtual concentration factor (i.e., Output/Input > 25) to ensure extracting ICRs (Hiranuma et al., 2016). **Fig. 2** shows temporal profiles of IS-PCVI experimental parameters during
40   the AIDA cloud simulation experiments. The number concentration of > 20 μm D_{ve} AIDA particles (i.e., above droplet-ice threshold size) was measured by the welas optical particle counter (Benz et al., 2005) virtually overlapped with our residual count (**Figs. 2d**). This comparability validated our choice of flow setting as well as resulting critical cut-size of IS-PCVI (> 24 µm).

2.8. Field mass concentration measurement. In this study, we used long-term data from a tapered-element oscillating
45   microbalance (TEOM; Thermo Scientific Inc., Model 1400a) (Patashnick and Rupprecht, 1991) deployed at a feedlot as an *in situ* aerosol particle mass concentration monitor to estimate ambient n_{INP}. Our TEOM was equipped with a PM_{10} inlet. With an operation flow of 16.7 lpm, our TEOM measured < 1 g m^{-3} of PM with a 5-minute time resolution. Two identical TEOMs were deployed at the upwind and downwind location of FY I as illustrated in Upadhyay et al. (2008), and they were kept running continuously during the entire 2016-2019 study period. The screened TEOM data were used as ambient particle emission data to
50   estimate INP concentration from a feedlot.

To complement the TEOM measurements and our aerosol particle sampling activities at each field, simultaneous mass concentration measurements of PM_{10} were also carried out at both downwind and upwind edges using DustTrak continuous particulate monitors (TSI Inc., Model 8520). The time series of upwind and downwind particle mass concentrations were measured by DustTrak instruments equipped with a PM_{10} inlet (not shown). Our TEOM measurement time resolution is 5 min, and some
55   data are patchy due to maintenance periods. Nevertheless, it is noteworthy that our TEOM and DustTrak PM_{10} measurements, conducted in a side-by-side position, agree within ± 40% on average. The often-observed downwind particle concentration of ≥ 1000 µg m^{-3} (> 10^{-6} g L^{-1}) is consistent with previous studies (Bush et al., 2014; Hiranuma et al., 2011). On the other hand, the observed mass concentration at the upwind sites was typically substantially lower, < 100 µg m^{-3} (or < 10^{-7} g L^{-1}), except for known/recorded interruptions (e.g., a car passing by), resulting in transient increase in mass concentration. We note that, as part of

our TEOM data screening and evaluation protocol, all systematic errors (i.e., mass concentration outside of measurable limits, noise > 100%, 3.5 lpm < main flow < 2.5 lpm, and 14 lpm < sheath flow < 13 lpm) were excluded from our data analysis.

5 In 2017, an optical particle sizer (OPS; TSI Inc., 3330) was used to measure particle size distributions at FY I–III. The time series of upwind and downwind particle size distributions measured by OPS (not shown) are very similar to our previous observation in 2008 (Fig. 5 of Hiranuma et al, 2011). We carried out the OPS measurements at the upwind site at the beginning and the end of dust sampling periods using an identical instrument. As can be seen in Fig. 5 of Hiranuma et al. (2011), while supermicron particles prevailed at the downwind site, the submicron population dominated at the upwind site, indicating that the observed supermicron ambient dust originated from a feedlot.

10 **2.9. IN parameterization method.** All IN data based on AIDA, WT-CRAFT, INSEKT, and DFPC were converted to and stored in INP concentration per unit standard air volume, particle mass, and particle surface as a function of T; $n_{INP}(T)$, $n_m(T)$, and $n_{s,geo}(T)$, respectively (DeMott et al., 2017; Ullrich et al., 2017). Doing these conversions required only scaling measured or estimated $n_{INP}(T)$ from each method to aerosol particle mass or surface area parameters provided in **Tables 1–3**. A consistent data interpolation method is important to systematically compare immersion freezing data from different IN measurement 15 methodologies. In this study, we present T-binned-average IN data (i.e., 0.5°C bins) as for the lab and field IN data. By following the inter-comparison method described in our previous studies (Hiranuma et al., 2015), all lab data were binned/interpolated in a consistent manner using a 0.5°C resolution data.

3. Results and Discussion

3.1. Ambient INP spectra. To evaluate the immersion freezing efficiency of ambient samples, we inverted our WT-CRAFT-based INP measurements to ice-nucleating efficiency metrics, such as n_{INP}, n_m, and $n_{s,geo}$ (DeMott et al., 2017; Hiranuma et al., 2015). We note that the background freezing contribution of the field blank filter was negligible (< 3%) at Ts above -25°C. Regardless, to eliminate any possible artifacts in our WT-CRAFT data, we purposely limited our WT-CRAFT data analysis in the T range 25 between 0°C and -25°C and excluded any uncertain systematically erroneous data. Shown in **Fig. 3** is a compilation of $n_{s,geo}(T)$ and $n_{INP}(T)$ spectra for all of our WT-CRAFT measurements in 2017–2019 in part presented in Whiteside et al. (2018). As seen in the figure, our field $n_{s,geo}(T)$ spectra are comparable with the lab-derived immersion spectra of surface materials (**Sect. 3.2**) within the range of Min–Max for T > -25°C (at 0.5°C intervals), validating the atmospheric relevance of our controlled chamber experimental results. Without scaling to the surface area, $n_{INP}(T)$ spectra exhibited a wide range of INPs over three orders of 30 magnitude; e.g., -25°C (10.07 to > 10,000 L^{-1}).

More interestingly, we observed a prominent linear relationship between aerosol particle mass and INP number concentration (at -25°C, **Fig. 4a**). Convincingly, the INP scaled to the mass (n_m, **Fig. 4b**) shows a nearly constant value (~3 x 10^9 g^{-1}) hovering at -25°C (independent of particle mass concentration). These results imply the following: (1) ambient meteorological conditions, summarized in **Table 1**, might not be determining factors for INP concentrations; and (2) there is a predominance of 35 supermicron INPs from the feedlot, which dominates particle mass. Individual values of cumulative mass (derived from DustTrak measurements), n_{INP}, and n_m for each sampling date are provided in **Table 1**.

Overall, our offline measurements of ambient INP concentration using field filter samples collected in the field show more than several hundred INPs L^{-1} at below -20°C. More interestingly, there is a notable correlation between INP and ambient aerosol particle mass concentrations based on our 2016-2019 field study, which indicates the importance of large supermicron 40 aerosol particles as INPs. This motivates the need for further characterization of our OAF samples in a controlled-lab setting in order to identify what particulate size population (i.e., supermicron vs. submicron) triggers their IN in a controlled lab setting.

3.2. IN efficiencies of surface materials. Shown in **Fig. 5** are the $n_{s,geo}(T)$ spectra of TXD01 and TXD05 derived from the AIDA and INSEKT experiments in comparison to three reference spectra, O14, S16, and U17 (O'Sullivan et al., 2014; Steinke et al., 45 2016; Ullrich et al., 2017), as well as our previous field data (**Fig. 3**). Our $n_{s,geo}(T)$ spectra are composed of the results of two techniques, AIDA and INSEKT. Dry-heated samples were assessed by both techniques. Further, INSEKT was used to assess immersion freezing efficiency of wet-boiled samples (dry-heated vs. wet-boiled) as well as bulk TXD01 and TXD05 materials (filter suspension vs. bulk). We made sure to assess at least a few degrees of common T interval in a series of measurements to see if they agree and, if so, to stitch the results together. For each sample, the spectra nearly overlap each other at T ~ -22°C, verifying 50 their comparability and complementing features. Further, as seen in **Fig. 5**, our OAF spectra are comparable to the previous agricultural soil dust parameterization at relatively low T (e.g., the $n_{s,geo}$ value of 10^{10} m^{-2} at -26°C). At T above -20°C, TXD01 (bulk) appears to be more active than TXD05 beyond the $n_{s,geo}(T)$ uncertainty (± 39%), presumably due to the different sample source (**Fig. 5.ii**). Nonetheless, our AIDA-INSEKT results virtually fall within the range of our field-derived $n_{s,geo}(T)$ values, validating the atmospheric relevance of our lab results (regardless of varied particle size distributions and sample types; see **Table** 55 **3**). More interestingly, our comparison between non-heated vs. heated samples indicated no substantial suppression in IN ability by heating, especially for dry-heated samples. This heat-resistant feature of OAF samples may be due to their pre-exposure to dry, high ambient and soil T conditions (Cole et al., 2009). Further, our mass spectrometry analysis on these two subsets revealed no significant deviation in chemical compositions (**SI S1**). Complementarily, our metagenomics analysis also found no deviation in terms of bacteria and fungi speciation between dry-heated and non-heat-treated samples as discussed below.

3.3. Submicron vs. Supermicron INP. The DFPC instrument assessed IN abilities of TXD01 and TXD05 aerosol particles that have different size ranges. Prior to the DFPC measurement, the sampled filter was inserted onto a metal plate and covered with a smooth surface of paraffin in order to assure good thermal contact of the filter with the supporting substrate. Subsequently, the
5 paraffin was slightly heated and rapidly cooled in order to fill the filter pores. DFPC controled the Ts of the filter and the air, saturated with respect to finely-minced ice, with the flow continuously grazing the filter. Measurements were performed at water supersaturation, SS_w, of 2%, and T_{filter} of -18°C and -22°C. The supersaturation was calculated theoretically from vapor pressures of ice and water. The exposure time of the filter was 20 min to grow visible ice crystals on INPs at the considered RH and T. Use of the dynamic chamber circumvents some of the problems arising with the static chamber, e.g., that the moisture supply under
10 static conditions may be rather inadequate at a filter surface both in overcoming the effect of hygroscopic particles and in activating all potential INPs.

    Ice crystals formed on the membrane filter were visually assessed as a function of T (-18°C and -22°C) and SS_w. Our DFPC-derived $n_{s,geo}(T)$ values are shown in **Fig. 6**, superposed on our INSEKT data (adapted from **Fig. 5**). As seen, at the measured Ts, the DFPC data agreed reasonably well with the INSEKT results within our error ranges. As other analyses showed, the
15 difference between non-heated and dry-heated samples in terms of $n_{s,geo}(T)$ was not apparent from DFPC beyond the error ranges, constraining the heat resistivity of Texas agricultural dust simulants.

    IN ability of TXD samples was evaluated with both $n_{s,geo}(T)$ and n_{INP}. Note that we examined the submicron vs. supermicron INPs for n_{INP}. The $n_{s,geo}(T)$ represents the IN efficiency scaled to the surface area, and our PM$_1$ $n_{s,geo}(T)$ and supermicron $n_{s,geo}(T)$ were virtually identical, implying non-size dependent IN ability across the sizes evaluated in this study. **Table**
20 **4** summarizes the comparison of the submicron vs. supermicron INPs. Supermicron INP fraction, $[(n_{INP,total} - n_{INP,PM1}) / n_{INP,total}]$ x 100, shows that this fraction contributed 49.7% $\pm$ 6.0% (average $\pm$ standard error) of total INP for TXD samples at -18°C and -22°C. This highlights the importance of the coarse fraction in the INP population.

3.4. IN parameterization. The exponential fits for T-binned $n_{s,geo}(T)$ data of all lab and field measurements are summarized in
25 **Table 5**. Fit parameters, computationally optimized for given the best correlation coefficient (r) for each category are given in this table. As can be inferred from the table, the overall $\Delta\log(n_{s,geo})/\Delta T$ value is similar for all non-heated categories (0.20–0.42). This range of deviations is roughly similar to what we previously observed for supermicron IN active cellulose particles (0.26–0.40) (Hiranuma et al., 2019). Slightly higher $\Delta\log(n_{s,geo})/\Delta T$ values were observed for wet-boiled particles (0.59–0.61) than others may be indicative of an alternation in freezing efficiency via hydrolysis and discharge of ice-nucleating materials in wet-boiled samples
30 (Welti et al., 2014). Suppression of $n_{s,\,geo}$ for wet-boiled samples at T above -20°C can be found in **Fig. 5.ii**. Nonetheless, the observed consistency in the spectral slopes suggests that lab and field measurements exhibit similar IN above examined Ts. More importantly, this parameterization offers a simple representation of natural supermicron-dominant INPs (nearly half of OAF-INPs is supermicron in diameter; see **Sect. 3.3**) in a very simple manner. Since our immersion parameterization is solely a function of a single parameter, T, this parameterization can be easily incorporated in many model platforms in a computationally-friendly
35 manner.

3.5. Metagenomics analysis. Table 6 summarizes our results of metagenomics analysis. The diversity of the microbiome in the dust samples identified microorganisms common in soil, bovine manure, and inhabitants of the bovine rumen, as expected (detailed in **SI S3**). Interestingly, no known IN active species of microorganisms (active at Ts above -10ºC) were detected, although genera
40 of *Bacteria* (*Pseudomonas*) and *Fungi* (*Fusarium*, *Mortierella*) known to include species with IN activity were detected, albeit in negligible numbers. This insignificance of IN active microbiome and relatively high importance of non-biological supermicron particles as OAF-INPs are deemed valid. Unless otherwise, the observed strong mass dependency of OAF-INPs (**Fig. 4**) cannot be explained. We also found very little difference in the bacterial and eukaryotic metagenome in bulk and heat-treated dust samples (no data for *Archaea* were obtained from heat-treated dust samples). Heat treatment of dust samples at 100°C for 12 hours
45 apparently did not destroy the DNA in our samples, even though most microbial cells were killed. Thus, no notable difference after dry-heating was observed for both TXD01 and TXD05, representing an important negative result (**Table 6**). The diversity of the bacterial microbiome in both samples showed a considerable difference after aerosolization of dust in the AIDA cloud chamber and the subsequent IN experiments in simulated clouds. In aerosolized dust, a significant increase of desiccation-resistant *Actinobacteria* was observed in both samples. Further, we also identified a significant decrease of desiccation-non-resistant
50 *Proteobacteria*, *Firmicutes*, and *Bacteroides* in aerosolized particles (**Table 6**). This result implies that aerosolization and microbial dispersion in the atmosphere may alter microbiome diversity and population, at least for our samples. This unique effect was not observed for *Fungi* and *Archaea* (see **SI S3** for more details).

3.6. Ice residual analysis. A total of 1,259 particles in the diameter range of 0.2 to 3 µm were assessed through electron microscopy
55 for their physicochemical properties. All of our single particle analyses were carrid out with the following parameters; electron beam accelerating voltages of 15 keV, spot size of 50, and the working distance of 10mm. **Table 7** summarizes size properties of analyzed particles. The number of measured particles was limited depending on the particle availability on each substrate. Nevertheless, we looked into at least 100 particles for each sample type, as seen in the table. Out of these particles, the diameter of TXD01 (0.625 µm) particles was on average smaller than TXD05 (0.875 µm). This observation is consistent with our offline

particle characterizations (**Table 2**) and the AIDA size measurements (**Table 3**). For the samples used in this study, we could not identify any systematic differences between aerosol particles and residuals in terms of size. An exception was TXD01, where the mode diameter of residuals appeared to be larger than aerosol particles. Regardless, we found substantial fractions of supermicron diameter particles in TXD01 (28%) and TXD05 (44%).

5   Higher aspect ratios in residuals compared to aerosol particles were found for both TXD01 and TXD05 samples. This difference indicates a relative increase in non-spherical particles in residuals. In short, Hiranuma et al. (2008) found that quasi-spherical OAF particles were predominantly salt rich hygroscopic particles, whereas non-spherical amorphous particles were found to be organic-dominant with negligible hygroscopicity. Thus, our results imply the inclusion of non-hygroscopic particles as ice residuals.

10   Next, the elemental composition through energy dispersive X-ray spectroscopy analysis revealed some notable difference between aerosol particle samples and residual samples. In this study, we followed the H13 classification scheme to define particle types in the electron microscopy analysis (Hiranuma et al., 2013). Briefly, we semi-quantitatively assessed atomic weight percentage of Organic (C, N, O), Salt-rich (Na, Mg, K, P), Mineral-rich (Al, Si, Ca), and Other. We detected carbon in all particles exclusively, but a background signal from polycarbonate substrate film could not be separated and ruled out. **Table 8** shows the

15   summary of particle types based on their elemental compositions for samples used in this study. It should be noted that the "rich" used in the names of particle classes only indicates intensive characteristic peaks in the energy dispersive X-ray spectra, and > 99.9% of particles (except a few aluminosilicate particles) examined in this study were predominantly composed of carbon elements as organics-mixed particles. As seen in the table, an increase in exclusively organic fractions as well as a substantial decrease in salt-rich particles in residuals persisted for both TXD01 and TXD05 samples. The organic type fraction in heated-

20   aerosols is slightly smaller than that in non-heated aerosols. Nevertheless, the increase of organic type fraction for heated-ICRs implies an insignificant effect of heating as well as an importance of heat-resisting organics for immersion freezing of OAF materials. This observation supports the result in **Table 7**. The reduction in salt-rich particles percentage might be relevant to an increase in aspect ratio (Hiranuma et al., 2008). The observed relative increase in organic-including particles, which might be substantially less hygroscopic compared to salt-rich particles, is also indicative of the predominance of immersion freezing (rather

25   than condensation freezing) (Belosi and Santachiara, 2019) as an IN mechanism of OAF particles. Indeed, immersion is a dominant mechanism of IN in mixed-phase clouds (Hande and Hoose, 2017). Regardless, liquid cloud formation might be a prerequisite for activating OAF particles as ice crystals in the atmosphere.

        Finally, our attempts to analyze the size-resolved abundance of each composition class was not conclusive (not shown), possibly due to limitations in the small population examined. Nonetheless, finding no clear size-dependence of elemental

30   compositions in both total aerosol and residual samples was an important negative result, which is consistent with findings through aerosol single particle spectrometry (**SI S1**).

3.7. Estimated INPs released from a feedyard. Upon a confirmation of comparability between field and lab $n_{s,geo}(T)$ values, we proceeded with ambient n_{INP} estimation based on our field mass concentration data. **Figure 7** summarizes the TEOM mass

35   concentration measured at the downwind side of FY I as well as cumulative INP concentrations estimated at Ts of -15°C, -20°C and -25°C. The background mass concentration measured at the upwind location (avg. ± std. error. = 2.24 x 10^{-8} ± 1.42 x 10^{-10} g L^{-1}) is shown in a red dashed line in **Fig. 7a** and subtracted from the downwind data. The resulting downwind concentration was on average is 4.12 x 10^{-7} ± 2.96 x 10^{-9} g L^{-1} (or 411.57 ± 2.96 μg m^{-3}), indicated in a blue dashed line in **Fig. 7a**. On average, the downwind concentration exhibited higher mass concentration by more than an order of magnitude. This result implies a constant

40   high particle load from the FY, which was also seen in a previous study at FY I (Hiranuma et al., 2011; Bush et al., 2014). Seasonal variation is also seen in **Fig. 7a**, as the annual peak of mass concentration (> 10^{-5} g L^{-1}) coincided with summer in each case. **Figure 7b** shows associated INP concentration estimations. To estimate n_{INP}, we first used the $n_{s,geo}(T)$ parameterization given in **Table 5** (**Eqn. *Field_Median***) to compute $n_{s,geo}(T)$. To convert $n_{s,geo}$ to n_{INP}, we have adapted Equations (1)-(3) in Hiranuma *et al*. (2015). Briefly, the measured mass concentration as well as field *SSA* were used to convert from $n_{s,geo}(T)$ to $n_{INP}(T)$:

45     $$n_{INP}(T)(L^{-1}) = n_{s,geo}(T)(m^{-2}) \times Geometric\ SSA \left(\frac{m^2}{g}\right) \times Mass\ Conc.\left(\frac{g}{L}\right).\qquad(1)$$

where the geometric *SSA* value for field data, approximately 0.4 m^2 g^{-1}, is derived from particle size distribution measurements presented in Fig. 3 of Hiranuma et al. (2011). As seen in **Fig. 7b**, average estimated INPs at three different Ts, -15°C, -20°C, and -25°C, are shown as a gray dashed line, black dashed line and black solid line, respectively. Our results show that the aerosol particles downwind of a feedlot contain several thousand INPs L^{-1} (median = 1,656 L^{-1}; average = 5,251 L^{-1}) at standard T and

50   pressure (STP) at -25°C, which is three orders of magnitude higher than typical ambient INP concentration from continental sources as reported in DeMott et al. (2010).

        While fine submicron mode might dominate number concentrations of aerosol particles at cloud heights, the presence of supermicron particles in clouds is evident over the arid Southwestern U.S. (Pinnick et al., 1993). This existence of supermicron particles at cloud altitudes is especially non-negligible when we consider atmospheric immersion freezing, which initiates on the

55   surface of a few in million particles. Our lab and field measurements-based parameterizations open up further study opportunities of incorporating supermiscron INPs from agricultural source in the atmospheric modeling simulation and may provide a hint to reveal the identity of INPs at relatively high Ts (> -15 °C).

4. Summary

Our AIDA and INSEKT controlled-experiments (immersion freezing) with OAF samples were successful, and we verified strong comparability of our field and controlled-lab results. Overall, we found that particle size is one of the most important particulate features of OAF dust, triggering immersion freezing in heterogeneous freezing Ts. In fact, supermicrometer OAF particles are responsible for nearly 50% of measured INPs. Due to the observed predominance of supermicron OAF particles, a substantially high number of INPs from feedlots (several thousands of INPs L^{-1} at -25°C) is expected. Ambient meteorological conditions seemed to not be determining factors for INP concentrations and emissions. But, higher time and bin resolutions as well as vertical profiles are necessary to further verify size-related statistics. The predominance of organics with salt contents (e.g., potassium) in OAF particle composition is consistent with our previous study of TXD particle composition analyses (Hiranuma et al., 2011). Further, ICR analysis revealed an increase in organic inclusion (and decrease in salt inclusion) in residuals, highlighting the importance of organic material for atmospheric immersion to be OAF-derived INPs. The insignificance of dry-heating was demonstrated with the increase of organics found for the ICR of dry-heated samples (**Table 8**) as well as the nearly identical shape of INP spectra for non-heated and heated samples (**Fig. 5**). Other properties were size independent and might not be relevant OAF-IN. We found no notable biological INPs, and the OAF samples and particles used in this study were heat tolerant with respect to IN potential. Thus, we conclude that the observed variability of 3–4 orders of magnitude at a single T could be explained by differences in these inherent physicochemical properties (i.e., size and non-proteinaceous organic fraction), which may in part explain a previously observed gap between online and offline IN measuring systems (Hiranuma et al., 2015). Developing an atmospheric IN parameterization based on findings in this study offers an efficient representation of natural, supermicron-dominant INPs. Due to its simplicity, our new parameterization can be used for atmospheric-modeling applications at any scale. Our OAF INP parameterization should be included in atmospheric models and compared to nucleation theory and empirical IN parameterization (Phillips et al., 2013). Currently, ice formation processes are poorly represented in the climate models, and more studies will help to fill this gap, especially in the U.S. Southern High Plains region. Further research should focus on understanding how organic composition influence IN. Our previous work using Raman micro-spectroscopy revealed that ambient dust sampled at OAFs is composed of brown or black carbon, hydrophobic humic acid, water soluble organics, less soluble fatty acids, and carbonaceous materials mixed with salts and minerals. But, our current knowledge regarding IN active organics is still limited. While we could not rule out the possibility of IN of TXD triggered by biological INPs, our current results did not support it. In the future, we also need to carry out an identical metagenomics analysis for ICR samples collected at various Ts. Extracting enough DNA out of ICR samples would be challenging and is currently not feasible at the AIDA facility. Facilitating a dynamic cooling expansion chamber, and collecting ICRs for a prolonged expansion experiment period would be a potential resolution. Moreover, our metagenomics analysis indicated that most microorganisms were alive, but it did not provide any quantitative percentage. Therefore, we must do metatranscriptomics (analysis of RNA) in the future, as only live organisms produce RNA. More interdisciplinary, collaborative studies (e.g., how the diet of cattle - inclusion of antibiotics, probiotics etc. - influences INP abundance in samples of feedlot surface materials) would also be useful.

Data availability. Original data created for the study are or will be available in a persistent repository upon publication (https://issues.pangaea.de/browse/PDI-25320 or West Texas A&M research web).

Supplement. The supplement related to this article is available online at: www.atmospheric-chemistry-and-physics.net

Author contributions. N.H., B.W.A, and N.U. designed research; N.H., B.W.A., F.B., J.B., K.C., D.G., K.H., Y.H., H.S., X.S., I.S., N.U., F.V., and O.M. performed research; N.H., F.B., R.F., D.G., K.H., Y.H., G.S., X.S., I.S., N.U., H.S.K.V., F.V., and O.M. analyzed data; and N.H., F.B., D.G., and X.S. wrote the paper.

Competing interests. The authors declare no conflict of interest.

Acknowledgments. This project has received funding from the European Union's Horizon 2020 research and innovation programme through the EUROCHAMP-2020 Infrastructure Activity under grant agreement No 730997. This material is based upon work supported by the U.S. Department of Energy, Office of Science, Office of Biological and Environmental Research under Award Number DE-SC-0018979. Naruki Hiranuma and Yidi Hou thank the Killgore Faculty Research and President's Undergraduate Student Research Grants.

References

- Angly, F.E., Dennis, P.G., Skarshewski, A., Vanwonterghem, I., Hugenholtz, P., and Tyson, G. W.: CopyRighter: a rapid tool for improving the accuracy of microbial community profiles through lineage-specific gene copy number correction, Microbiome., 2, 11, 2014.
- Atkinson, J. D., Murray, B. J., Woodhouse, M. T., Whale, T.F., Baustian, K. J., Carslaw, K. S., Dobbie, S., O'Sullivan, D., and Malkin, T. L.: The importance of feldspar for ice nucleation by mineral dust in mixed-phase clouds, Nature, 498, 355–358, 2013.
- Belosi, F. and Santachiara, G.: Laboratory investigation of aerosol coating and capillarity effects on particle ice nucleation in deposition and condensation modes, Atmos. Res., 230, 104633, 2019.
- Benz, S., Megahed, K., Möhler, O., Saathoff, H., Wagner, R., and Schurath, U.: T-dependent rate measurements of homogeneousice nucleation in cloud droplets using a large atmospheric simu-lation chamber, J. Photoch. Photobio. A, 176, 208–217, 2005.
- Boose, Y., Welti, A., Atkinson, J., Ramelli, F., Danielczok, A., Bingemer, H. G., Plötze, M., Sierau, B., Kanji, Z. A., and Lohmann, U.: Heterogeneous ice nucleation on dust particles sourced from nine deserts worldwide – Part 1: Immersion freezing, Atmos. Chem. Phys., 16, 15075–15095, 2016.
- Boulter, J. E., Cziczo, D. J., Middlebrook, A. M., Thomson, D. S., and Murphy, D. M.: Design and performance of a pumped counterflow virtual impactor, Aerosol. Sci. Technol., 40, 969–976, 2006.
- Brunauer, S., Emmett, P. H., and Teller, E.: Adsorption of gases in multimolecular layers, J. Am. Chem. Soc., 60, 309–319, 1938.
- Bush, J., Heflin, K. R., Marek, G. W., Bryant, T. C., and Auvermann, B. W.: Increasing stocking density reduces emissions of fugitive dust from cattle feedyards, Applied Engineering in Agriculture, 30, 815–824, 2014.
- Cole, N. A., Mason, A. M., Todd, R. W., Rhoades, M., and Parker, D. B.: Chemical composition of pen surface layers of beef cattle feedyards, Professional Animal Scientist, 25, 541–552, 2009.
- Cory, K. M.: Immersion freezing of non-proteinaceous biological aerosol proxies & Arctic ambient particles, M. S. thesis, West Texas A&M University, https://wtamu-ir.tdl.org/handle/11310/227, 66 pp., 2019.
- DeMott, P. J., Prenni, A. J., Liu, X., Kreidenweis, S. M., Petters, M. D., Twohy, C. H., Richardson, M. S., Eidhammer, T., and Rogers, D. C.: Predicting global atmospheric ice nuclei distributions and their impacts on climate, Proc. Natl. Acad. Sci. U.S.A., 107, 11217–11222, 2010.
- DeMott, P. J., Hill, T. C. J., Petters, M. D., Bertram, A. K., Tobo, Y., Mason, R. H., Suski, K. J., McCluskey, C. S., Levin, E. J. T., Schill, G. P., Boose, Y., Rauker, A. M., Miller, A. J., Zaragoza, J., Rocci, K., Rothfuss, N. E., Taylor, H. P., Hader, J. D., Chou, C., Huffman, J. A., Pöschl, U., Prenni, A. J., and Kreidenweis, S. M.: Comparative measurements of ambient atmospheric concentrations of ice nucleating particles using multiple immersion freezing methods and a continuous flow diffusion chamber, Atmos. Chem. Phys., 17, 11227–11245, 2017.
- DeMott, P. J., Mason, R. H., McCluskey, C. S., Hill, T. C. J., Perkins, R. J., Desyaterik, Y., Bertram, A. K., Trueblood, J. V., Grassian, V. H., Qiu, Y., Molinero, V., Tobo, Y., Sultana, C. M., Christopher, L., and Prather, K. A.: Ice nucleation by particles containing long-chain fatty acids of relevance to freezing by sea spray aerosols, Environmental Science: Processes & Impacts, 20, 1559–1569, 2018.
- Després, V. R., Huffman, J. A., Burrows, S. M., Hoose, C., Safatov, A. S., Buryak, G., Fröhlich-Nowoisky, J., Elbert, W., Andreae, M. O., Pöschl, U., and Jaenicke, R.: Primary biological aerosols in the atmosphere: A review of observations and relevance, Tellus B, 64, 15598, 2012.
- Drouillard, J. S.: Current situation and future trends for beef production in the United States of America - A review, Asian-Australas J Anim Sci., 31, 1007–1016, 2018.
- Duniway, M. C., Pfennigwerth, A. A., Fick, S. E., Nauman, T. W., Belnap, J., and Barger, N. N.: Wind erosion and dust from US drylands: a review of causes, consequences, and solutions in a changing world, Ecosphere, 10, 2019.
- Edgar, R. C., Haas, B. J., Clemente, J. C., Quince, C., and Knight, R.: UCHIME improves sensitivity and speed of chimera detection. Bioinformatics, 27, 2194–2200, 2011.
- Eren, A. M., Maignien, L., Sul, W. J., Murphy, L. G., Grim, S. L., Morrison, H. G., and Sogin, M. L.: Oligotyping: differentiating between closely related microbial taxa using 16s rRNA gene data. Methods, Ecol. Evol., 4, 1111–1119, 2013.
- Eren, A. M., Morrison, H. G., Lescault, P. J., Reveillaud, J., Vineis, J. H., and Sogin, M. L.: Minimum entropy decomposition: Unsupervised oligotyping for sensitive partitioning of high-throughput marker gene sequences, The ISME Journal, 9, 968–979, 2015.
- Ginoux, P., Prospero, J. M., Gill, T. E., Hsu, N. C., and Zhao, M.: Global scale attribution of anthropogenic and natural dust sources and their emission rates based on modis deep blue aerosol products, Rev. Geophys., 50, RG3005, 2012.

- Hande, L. B. and Hoose, C.: Partitioning the primary ice formation modes in large eddy simulations of mixed-phase clouds, Atmos. Chem. Phys., 17, 14105–14118, 2017.
- Hill, T. C., Moffett, B. F., DeMott, P. J., Georgakopoulos, D. G., Stump, W. L., and Franc, G. D.: Measurement of ice nucleation-active bacteria on plants and in precipitation by quantitative pcr, Appl. Environ. Microbiol., 80, 1256–1267, 2014.
- Hill, T. C., DeMott, P. J., Tobo, Y., Fröhlich-Nowoisky, J., Moffett, B. F., Franc, G. D., and Kreidenweis, S. M.: Sources of organic ice nucleating particles in soils, Atmos. Chem. Phys., 16, 7195–7211, 2016.
- Hiranuma, N., Brooks, S. D., Auvermann, B. W., and Littleton, R.: Using environmental scanning electron microscopy to determine the hygroscopic properties of agricultural aerosols, Atmos. Environ., 42, 1983–1994, 2008.
- Hiranuma, N., Brooks, S. D., Gramann, J., and Auvermann, B. W.: High concentrations of coarse particles emitted from a cattle feeding operation, Atmos. Chem. Phys., 11, 8809–8823, 2011.
- Hiranuma, N., Brooks, S. D., Moffet, R. C., Glen, A., Laskin, A., Gilles, M. K., Liu, P., Macdonald, A. M., Strapp, J. W., and McFarquhar, G. M.: Chemical characterization of individual particles and residuals of cloud droplets and ice crystals collected on board research aircraft in the ISDAC 2008 study, J. Geophys. Res.-Atmos., 118, 6564–6579, 2013.
- Hiranuma, N., Augustin-Bauditz, S., Bingemer, H., Budke, C., Curtius, J., Danielczok, A., Diehl, K., Dreischmeier, K., Ebert, M., Frank, F., Hoffmann, N., Kandler, K., Kiselev, A., Koop, T., Leisner, T., Möhler, O., Nillius, B., Peckhaus, A., Rose, D., Weinbruch, S., Wex, H., Boose, Y., DeMott, P. J., Hader, J. D., Hill, T. C. J., Kanji, Z. A., Kulkarni, G., Levin, E. J. T., McCluskey, C. S., Murakami, M., Murray, B. J., Niedermeier, D., Petters, M. D., O'Sullivan, D., Saito, A., Schill, G. P., Tajiri, T., Tolbert, M. A., Welti, A., Whale, T. F., Wright, T. P., and Yamashita, K.: A comprehensive laboratory study on the immersion freezing behavior of illite NX particles: a comparison of 17 ice nucleation measurement techniques, Atmos. Chem. Phys., 15, 2015.
- Hiranuma, N., Möhler, O., Kulkarni, G., Schnaiter, M., Vogt, S., Vochezer, P., Järvinen, E., Wagner, R., Bell, D. M., Wilson, J., Zelenyuk, A., and Cziczo, D. J.: Development and characterization of an ice-selecting pumped counterflow virtual impactor (IS-PCVI) to study ice crystal residuals, Atmos. Meas. Tech., 9, 3817–3836, 2016.
- Hiranuma, N., Adachi, K., Bell, D. M., Belosi, F., Beydoun, H., Bhaduri, B., Bingemer, H., Budke, C., Clemen, H.-C., Conen, F., Cory, K. M., Curtius, J., DeMott, P. J., Eppers, O., Grawe, S., Hartmann, S., Hoffmann, N., Höhler, K., Jantsch, E., Kiselev, A., Koop, T., Kulkarni, G., Mayer, A., Murakami, M., Murray, B. J., Nicosia, A., Petters, M. D., Piazza, M., Polen, M., Reicher, N., Rudich, Y., Saito, A., Santachiara, G., Schiebel, T., Schill, G. P., Schneider, J., Segev, L., Stopelli, E., Sullivan, R. C., Suski, K., Szakáll, M., Tajiri, T., Taylor, H., Tobo, Y., Ullrich, R., Weber, D., Wex, H., Whale, T. F., Whiteside, C. L., Yamashita, K., Zelenyuk, A., and Möhler, O.: A comprehensive characterization of ice nucleation by three different types of cellulose particles immersed in water, Atmos. Chem. Phys., 19, 4823–4849, 2019.
- Hoose, C. and Möhler, O.: Heterogeneous ice nucleation on atmospheric aerosols: a review of results from laboratory experiments, Atmos. Chem. Phys., 12, 9817–9854, 2012.
- Katra, I.: Soil erosion by wind and dust emission in semi-arid soils due to agricultural activities, Agronomy, 10, 89, 2020.
- Kenny, L. C., Gussman, R., and Meyer, M.: Development of a sharp-cut cyclone for ambient aerosol monitoring applications, Aerosol. Sci. Technol., 32, 338–358, 2000.
- Kiselev, A., Bachmann, F., Pedevilla, P., Cox, S.J., Michaelides, A., Gerthsen, D., and Leisner, T.: Active sites in heterogeneous ice nucleation – the example of K-rich feldspars, Science, 355, 367–371, 2017.
- Langer, G. and Rodgers, J.: An experimental study of ice nuclei on membrane filters and other substrata, J. Appl. Meteorol., 14, 560–571, 1975.
- Li, R., Dong, X., Guo, J., Fu, Y., Zhao, C., Wang, Y., and Min, Q.: The implications of dust ice nuclei effect on cloud top temperature in a complex mesoscale convective system, Scientific Reports, 7, 13826, 2017.
- Möhler, O., Stetzer, O., Schaefers, S., Linke, C., Schnaiter, M., Tiede, R., Saathoff, H., Krämer, M., Mangold, A., Budz, P., Zink, P., Schreiner, J., Mauersberger, K., Haag, W., Kärcher, B., and Schurath, U.: Experimental investigation of homogeneous freezing of sulphuric acid particles in the aerosol chamber AIDA, Atmos. Chem. Phys., 3, 211–223, 2003.
- Nagaraja, T. G.: in Rumenology, edited by: Millen, D., De Beni Arrigoni, M., and Lauritano Pacheco, R., Springer, pp. 39–61, 2016.
- O'Sullivan, D., Murray, B. J., Malkin, T. L., Whale, T. F., Umo, N. S., Atkinson, J. D., Price, H. C., Baustian, K. J., Browse, J., and Webb, M. E.: Ice nucleation by fertile soil dusts: relative importance of mineral and biogenic components, Atmos. Chem. Phys., 14, 1853–1867, 2014.
- Overpeck, J. T. and Udall, B.: Climate change and the aridification of North America, Proc. Natl. Acad. Sci. U.S.A., 117, 11856–11858, 2020.
- Patashnick, H. and Rupprecht, E. G.: Continuous PM-10 measurements using the tapered element oscillating microbalance, Journal of the Air and Waste Management Association, 41, 1079–1083, 1991.

- Perkins, R. J., Gillette, S. M., Hill, T. C. J., and Demott, P. J.: The labile nature of ice nucleation by Arizona Test Dust, ACS Earth Sp Chem. 4, 133–141, 2020.
- Phillips, V. T. J., DeMott, P. J., Andronache, C., Pratt, K. A., Prather, K. A., Subramanian, R., and Twohy, C.: Improvements to an empirical parameterization of heterogeneous ice nucleation and its comparison with observations, J. Atmos. Sci., 70, 378–409, 2013.
- Pinnick, R. G., Fernandez, G., Martinez-Andazola, E., Hinds, B. D., Hansen, A. D. A., and Fuller, K.: Aerosol in the arid southwestern United States: Measurements of mass loading, volatility, size distribution, absorption characteristics, black carbon content, and vertical structure to 7 km above sea level, *J. Geophys. Res.*, 98, 2651–2666, 1993.
- Rognes, T., Flouri, T., Nichols, B., Quince, C., and Mahé, F.: VSEARCH: a versatile open source tool for metagenomics, PeerJ. 4, e2584, 2016.
- Santachiara, G., Di Matteo, L., Prodi, F., and Belosi, F.: Atmospheric particles acting as ice forming nuclei in different size ranges, Atmos. Res., 96, 266–272, 2010.
- Schiebel, T.: Ice nucleation activity of soil dust aerosols, Ph.D. thesis, Karlsruhe Institute of Technology, https://doi.org/10.5445/IR/1000076327, 131 pp., 2017.
- Schneider, J., Höhler, K., Heikkilä, P., Keskinen, J., Bertozzi, B., Bogert, P., Schorr, T., Umo, N. S., Vogel, F., Brasseur, Z., Wu, Y., Hakala, S., Duplissy, J., Moisseev, D., Kulmala, M., Adams, M. P., Murray, B. J., Korhonen, K., Hao, L., Thomson, E. S., Castarède, D., Leisner, T., Petäjä, T., and Möhler, O.: The seasonal cycle of ice-nucleating particles linked to the abundance of biogenic aerosol in boreal forests, Atmos. Chem. Phys. Discuss., https://doi.org/10.5194/acp-2020-683, in review, 2020.
- Steinke, I., Funk, R., Busse, J., Iturri, A., Kirchen, S., Leue, M., Möhler, O., Schwartz, T., Schnaiter, M., Sierau, B., Toprak, E., Ullrich, R., Ulrich, A., Hoose, C., and Leisner, T.: Ice nucle-ation activity of agricultural soil dust aerosols from Mongolia, Argentina, and Germany, J. Geophys. Res.-Atmos., 121, 13559–13576, 2016.
- Steinke, I., Hiranuma, N., Funk, R., Höhler, K., Tüllmann, N., Umo, N. S., Weidler, P. G., Möhler, O., and Leisner, T.: Complex plant-derived organic aerosol as ice-nucleating particles – more than the sums of their parts?, Atmos. Chem. Phys., 20, 11387–11397, 2020.
- Suski, K. J., Hill, T. C. J., Levin, E. J. T., Miller, A., DeMott, P. J., and Kreidenweis, S. M.: Agricultural harvesting emissions of ice-nucleating particles, Atmos. Chem. Phys., 18, 13755–13771, 2018.
- Tobo, Y.: An improved approach for measuring immersion freezing in large droplets over a wide temperature range, Sci. Rep. 6, 32930, 2016.
- Ullrich, R., Hoose, C., Möhler, O., Niemand, M., Wagner, R., Höhler, K., Hiranuma, N., Saathoff, H., and Leisner, T.: A new icenucleation active site parameterization for desert dust and soot, J. Atmos. Sci., 74, 699–717, 2017.
- Upadhyay, J., Auvermann, B. W., Paila, A. N., and Hiranuma, N.: Open-path transmissometry to determine the atmospheric extinction efficiency of feedyard dust, Transactions of the ASABE, 51, 1433–1441, 2008.
- Vali, G., DeMott, P. J., Möhler, O., and Whale, T. F.: Technical Note: A proposal for ice nucleation terminology, Atmos. Chem. Phys., 15, 10263–10270, 2015.
- Von Essen, S. G. and Auvermann, B. W.: Health effects from breathing air near CAFOs for feeder cattle or hogs, J Agromedicine, 10, 55–64, 2005.
- Welti, A., Kanji, Z. A., Lüönd, F., Stetzer, O., and Lohmann, U.: Exploring the mechanisms of ice nucleation on kaolinite: from deposition nucleation to condensation freezing, J. Atmos. Sci. 71, 16–36, 2014.
- Westbrook, C. D. and Illingworth, A. J.: Evidence that ice forms primarily in supercooled liquid clouds at temperatures > −27°C, Geophys. Res. Lett., 38, L14808, 2011.
- Whiteside, C. L., Auvermann, B. W., Bush, J., Goodwin, C., McFarlin, R., and Hiranuma, N.: Ice nucleation activity of dust particles emitted from cattle feeding operations in the Texas Panhandle, Poster, AMS - 10th Symposium on Aerosol-Cloud-Climate Interactions, Austin, TX, USA, doi: 10.13140/RG.2.2.29505.38248, 2018.

Figures and Tables
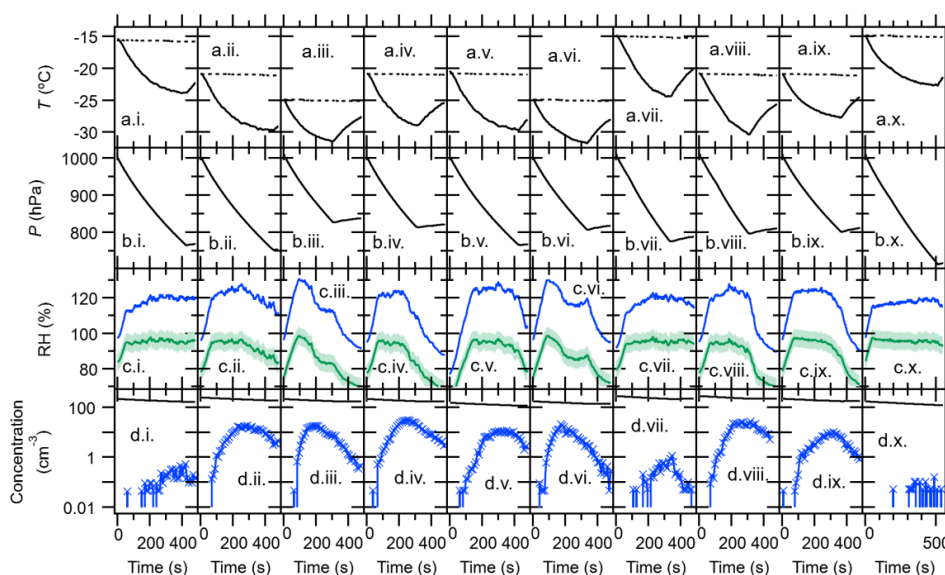
Figure 1. Temporal profiles of the AIDA immersion freezing experiment [TXDUST01_07 (i), _08 (ii), _30 (iii), _12 (iv), _13 (v), _32 (vi), _3 (vii), _4 (viii), _16 (ix), _17 (x)]. Arrays of alphabetical panels represent the chamber gas T (solid line) and the chamber wall T (dashed line) (a), P in the AIDA chamber vessel (b), RH with respect to water (green line) and ice (blue line) (c), and aerosol particle concentration initially measured by the CPC (black solid line) as well as number concentration of > 20 μm D_{ve} AIDA particles measured by a welas optical particle counter (blue line) (d). Horizontal numerical panels represent different sample types and AIDA experiments, including TXD01 (i)–(iii), TXD05 (iv)–(vi), TXD01H (vii–viii), and TXD05H (ix–x). RHs were determined with an accuracy of ± 5% using the mean gas T and the mean water vapor concentration.
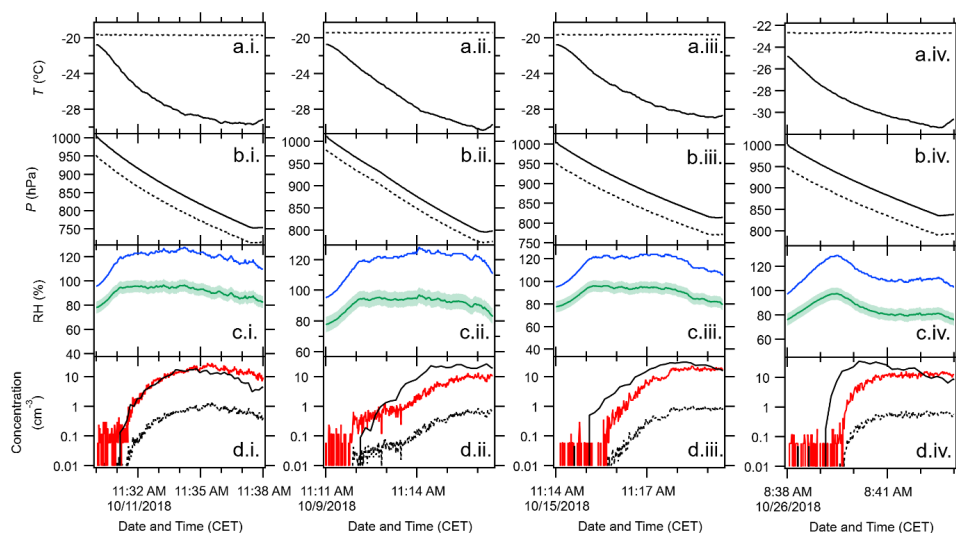
Figure 2. Temporal plots of the AIDA freezing experiment. Arrays of alphabetical panels represent the chamber gas T (solid line) and the IS-PCVI nozzle T (dashed line) (a), P in the AIDA chamber (solid line) and the IS-PCVI (dashed line) (b), RH with respect to water (green line) and ice (blue line) (c), and residuals measured by the CPC (red solid line) and corrected residual concentration according to Eqn. (6) of Hiranuma et al. (2016) (black dashed line) (d). In Panel (d), the number concentration of > 20 µm D_{ve} AIDA particles measured by the welas optical particle counter (black solid line) is also shown. Horizontal numerical panels represent different sample types and AIDA experiments, including TXD01 (TXDUST01_08) (i), dry-heated TXD01 (TXDUST01_04) (ii), TXD05 (TXDUST01_12) (iii), and dry-heated TXD05 (TXDUST01_31) (iv). RHs were determined with an accuracy of ± 5% using the mean gas T and the mean water vapor concentration. Note that the minimum detection of CPC is 0.1 cm^{-3}, and only negligible background particle concentration was observed prior to each expansion. The CF-to-IF ratios of 0.180 (ii) and 0.136 (i, iii and iv) correspond to critical ice particle cut-sizes of > 24 µm volume-equivalent diameter, according to Fig. 9 of Hiranuma et al. (2016), transmitting pristine ice crystals downstream of the IS-PCVI.
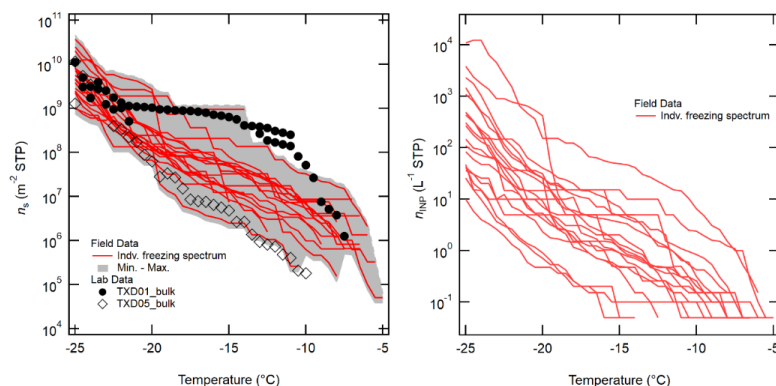
Figure 3. The $n_{s,geo}(T)$ spectra (a) and $n_{INP}(T)$ spectra (b) of FY samples. The gray shaded area represents the minimum and maximum $n_{s,geo}(T)$ values (CI95% values included) with the 0.5°C T interval. A subset of lab $n_{s,geo}(T)$ spectral data discussed in **Sect. 3.2** (i.e., TXD01_bulk and TXD05_bulk), composed of the AIDA and INSEKT data, are superposed to guide the reader's eye.
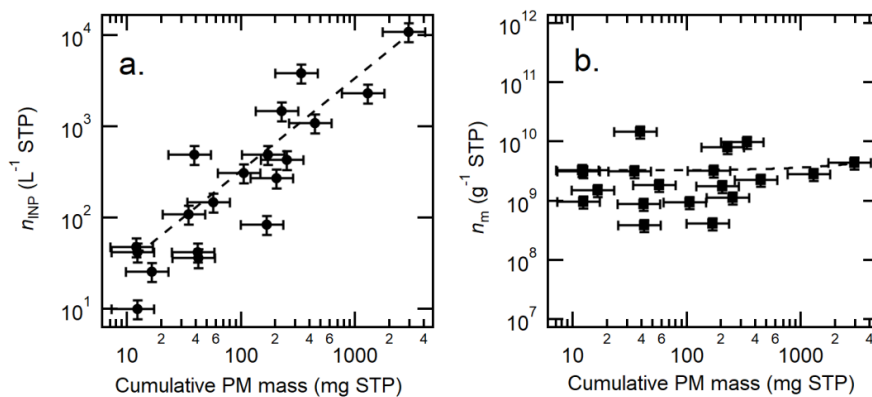
Figure 4. Correlation between cumulative PM mass vs. n_{INP} (a) and vs. n_m (b). Note the errors in cumulative PM mass are ± 40.4%, derived from calibration of two DustTrak instruments against TEOM in a side-by-side position. The uncertainty in n_{INP} and n_m is ± 23.5% (Hiranuma et al., 2019).
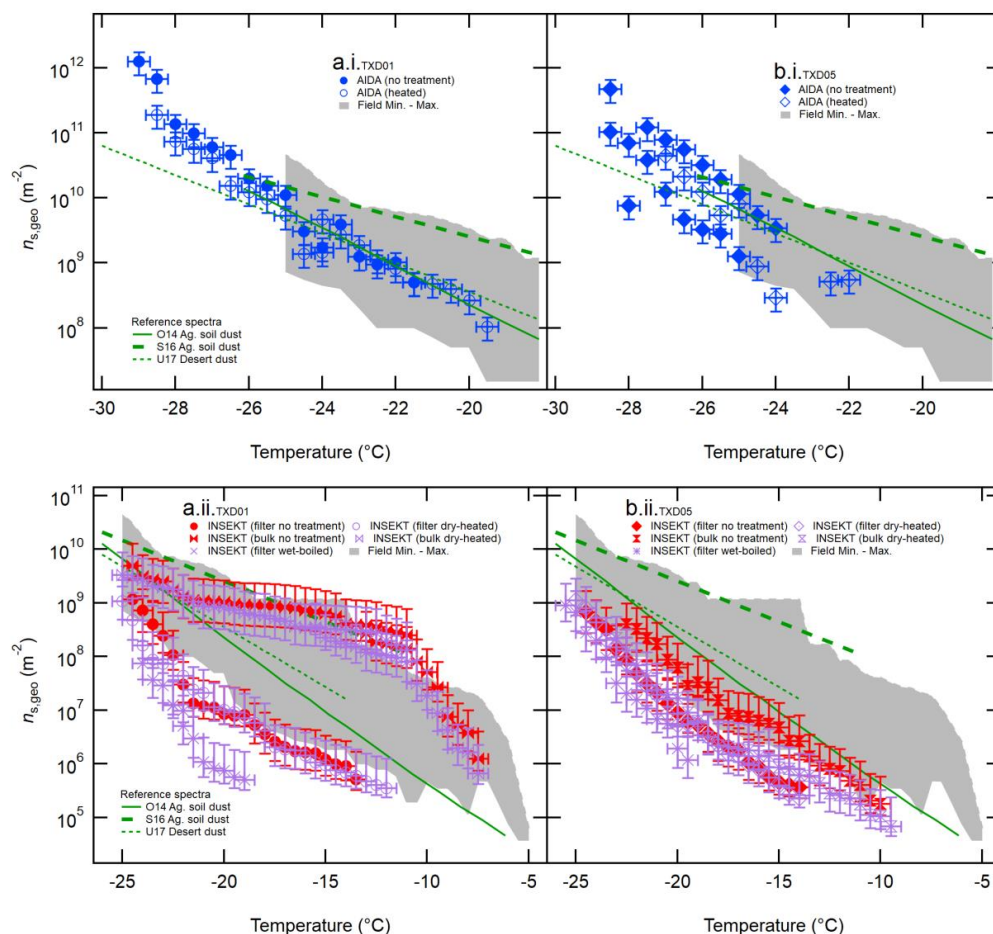
Figure 5. IN spectra of OAF aerosol particles. IN active surface-site density, $n_{s,geo}(T)$, of TXD01 (panel a) and TXD05 (panel b) assessed by AIDA (i) and INSEKT (ii) as a function of T. A comparison of the non-heat-treated sample to the heated-sample is shown. Three reference $n_{s,geo}(T)$ lines for similar dust samples are adapted from O'Sullivan et al. (2014; O14), Steinke et al. (2016; S16), and Ullrich et al. (2017; U17). The grey-shaded area represents the range of our field $n_{s,geo}(T)$ values at 0.5°C interval for -5°C > T > -25°C (**Fig. 3**).
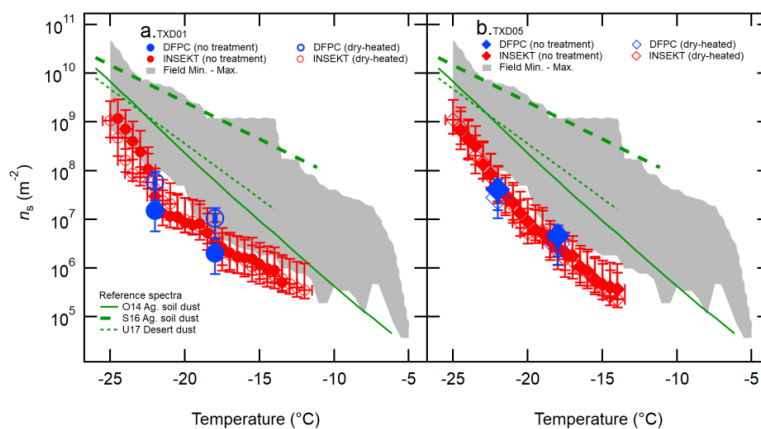
Figure 6. IN active surface-site density, $n_{s,geo}(T)$, of TXD01 (panel a) and TXD05 (panel b) measured by DFPC (Total) and INSEKT (adapted from **Fig. 5**). A comparison of non-heat-treated sample to dry-heated-sample for both instruments is shown. Three reference $n_{s,geo}(T)$ lines for similar dust samples are adapted from O14, S16, and U17.

5   The grey-shaded area represents the range of our field $n_{s,geo}(T)$ values at 0.5°C interval for -5°C > T > -25°C (**SI S1**).
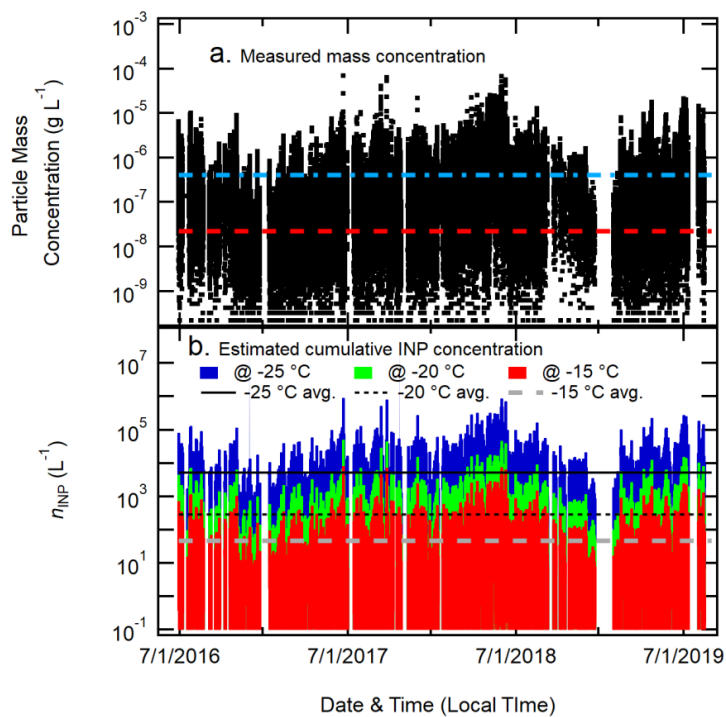
Figure 7. OAF-INP concentrations. Time-series plot of TEOM mass concentration measured at the downwind side of FY I (a) and cumulative INP concentrations estimated at Ts of -15°C, -20 °C, and -25°C (b).

Table 1. Summary of the ambient aerosol particle filter sampling conditions: UW denotes upwind.

Year	Date	Location	Start Time (Local)	End Time (Local)	Sample Flow (lpm)*	Total volume of sampled air (L STP)	T (°C)	P (mb)	Relative Humidity (%)
2019	20190715	FY I	18:45:00	22:05:00	4.19	838.0	30.1 ± 3.2	1015.6 ± 0.2	42.0 ± 10.8
	20190716	FY II	18:45:00	20:29:00	4.30	447.2	34.0 ± 0.7	1016.0 ± 0.2	27.8 ± 1.7
	20190724	FY III	19:24:00	20:34:00	9.08	317.8	28.9 ± 0.8	1020.6 ± 0.1	31.6 ± 1.4
	20190226	FY I	16:08:00	19:09:00	3.95	715.0	20.5 ± 2.7	1014.8 ± 0.2	14.3 ± 2.9
	20190328	FY II	16:26:00	20:52:00	5.00	1330.0	19.4 ± 1.5	1012.8 ± 0.2	26.5 ± 6.8
	20190420	FY III	17:05:00	21:05:00	4.15	996.0	27.0 ± 2.9	1009.0 ± 0.4	16.6 ± 5.0
	20190116	FY I	16:03:00	19:33:00	3.97	832.7	16.5 ± 1.9	1014.7 ± 0.4	30.3 ± 3.1
	20190117	FY II	15:48:00	19:30:00	3.97	880.2	11.0 ± 0.2	1016.9 ± 3.5	30.2 ± 5.6
	20190118	FY III	15:40:00	18:40:00	3.62	651.6	11.5 ± 3.9	1005.3 ± 2.2	41.1 ± 21.8
2018	20180722	FY I	18:42:00	22:39:00	6.58	1560.0	33.4 ± 4.3	1015.7 ± 0.3	17.8 ± 5.8
	20180723	FY II	18:42:00	22:17:00	5.46	1173.8	28.4 ± 2.2	1022.5 ± 0.7	39 ± 5.1
	20180724	FY III	18:20:00	22:13:00	3.65	850.3	28.9 ± 1.4	1023.3 ± 0.6	38.1 ± 2.6
	20180416	FY IV	16:53:30	20:06:40	5.99	1158.0	27.2 ± 1.3	1009.8 ± 8.0	5.6 ± 0.8
2017	20170709	FY I	19:32:45	22:26:00	5.28	915.6	27.9 ± 2.9	1017.0 ± 0.4	52.8 ± 13.1
	20170710	FY II	18:06:00	22:06:30	5.10	1227.2	30.5 ± 2.5	1015.5 ± 0.3	30.8 ± 5.1
	20170711	FY III	18:28:00	22:08:00	5.13	1128.0	29.9 ± 2.5	1015.2 ± 0.4	26.6 ± 6.0
	20170709	FY I-UW	19:50:00	22:47:00	5.28	935.2	27.9 ± 2.9	1017.0 ± 0.4	52.8 ± 13.1
	20170710	FY II-UW	18:28:00	22:24:00	5.10	1204.2	30.5 ± 2.5	1015.5 ± 0.3	30.8 ± 5.1
	20170711	FY III-UW	18:41:45	21:54:00	5.12	983.5	29.9 ± 2.5	1015.2 ± 0.4	26.6 ± 6.0

Year	Date	Location	Start Time (Local)	End Time (Local)	Cumulative PM mass (µg STP)†	n_{INP}@ -25°C (L⁻¹ STP)	n_m@ -25°C (g⁻¹ STP)
2019	20190715	FY I	18:45:00	22:05:00	168.2	8.38E+01	4.18E+08
	20190716	FY II	18:45:00	20:29:00	41.9	3.66E+01	3.91E+08
	20190724	FY III	19:24:00	20:34:00	105.0	3.11E+02	9.42E+08
	20190226	FY I	16:08:00	19:09:00	57.2	1.48E+02	1.84E+09
	20190328	FY II	16:26:00	20:52:00	204.5	2.72E+02	1.77E+09
	20190420	FY III	17:05:00	21:05:00	34.5	1.10E+02	3.18E+09
	20190116	FY I	16:03:00	19:33:00	12.0	4.78E+01	3.31E+09
	20190117	FY II	15:48:00	19:30:00	41.5	4.22E+01	8.94E+08
	20190118	FY III	15:40:00	18:40:00	251.8	4.35E+02	1.13E+09
2018	20180722	FY I	18:42:00	22:39:00	1281.0	2.31E+03	2.81E+09
	20180723	FY II	18:42:00	22:17:00	2917.9	1.10E+04	4.43E+09
	20180724	FY III	18:20:00	22:13:00	334.1	3.87E+03	9.84E+09
	20180416	FY IV	4:53:30	8:06:40	38.9	4.93E+02	1.47E+10
2017	20170709	FY I	19:32:45	22:26:00	445.3	1.09E+03	2.25E+09
	20170710	FY II	18:06:00	22:06:30	226.5	1.48E+03	8.00E+09
	20170711	FY III	18:28:00	22:08:00	171.5	4.92E+02	3.23E+09
	20170709	FY I-UW	19:50:00	22:47:00	12.4	4.22E+01	3.18E+09
	20170710	FY II-UW	18:28:00	22:24:00	12.4	1.01E+01	9.78E+08
	20170711	FY III-UW	18:41:45	21:54:00	16.5	2.57E+01	1.53E+09

*A mass flow controller or a critical orifice was used to ensure a constant flow throughout each sampling activity. An air flow rate was measured with a flowmeter (TSI Inc., Model 4140). †Cumulative values of mass collected on a filter were estimated by integrating DustTrak mass data, sampling time, and flow rate.

Table 2. Properties of OAF samples: non-heated (TXD01 & TXD05) and dry-heated (TXD01H & TXD05H).

System	TXD01	TXD05	TXD01H	TXD05H
[1]Density, g cm^{-3}	1.89 ± 0.06	2.05 ± 0.06	1.94 ± 0.06	2.00 ± 0.06
Geometric *SSA*, m^2 g^{-1}	4.95 ± 0.82	3.97 ± 0.02	5.62 ± 0.16	4.04 ± 0.11
[2]BET-based *SSA*, m^2 g^{-1}	3.23 ± 0.20	2.41 ± 0.20	3.23 ± 0.32	2.41 ± 0.24

[1]With a measurement relative standard deviation of ± 3%, our system is capable of measuring densities of other powder samples, such as illite NX (2.91 g cm^{-3}) and fibrous cellulose (1.62 g cm^{-3}). Note that these values are similar to the density values reported by manufacturers for illite NX (2.65 g cm^{-3}) and fibrous cellulose (1.5 g cm^{-3}). [2]Brunauer et al., 1938.

Table 3. Characterization of particle properties: assessed prior to AIDA expansion experiments (H denotes dry-heated).

Experiment ID	Aerosol Particle Type	Mode (Min–Max) Diameter, μm**	$N_{total,0}$, x10^3 L^{-1}	$S_{total,0}$, x10^{-9} m^2 L^{-1}	$M_{total,0}$, x10^{-9} g L^{-1}	Geometric SSA, m^2 g^{-1}
			Aerosol Particle Measurements			
TXDUST01_7	TXD01	0.55 (0.10–3.16)	213.7	98.8	18.4	5.38
TXDUST01_8*	TXD01	0.54 (0.11–2.69)	266.3	115.5	21.1	5.46
TXDUST01_30	TXD01	0.72 (0.08–6.44)	210.6	119.0	29.7	4.01
TXDUST01_12*	TXD05	0.67 (0.09–5.14)	199.2	163.5	41.1	3.98
TXDUST01_13	TXD05	0.71 (0.10–4.71)	155.0	117.2	29.6	3.95
TXDUST01_32	TXD05	0.84 (0.15–4.37)	163.3	124.9	33.2	3.77
TXDUST01_3*	TXD01H	0.53 (0.10–2.69)	301.1	130.5	23.7	5.51
TXDUST01_4	TXD01H	0.52 (0.08–3.05)	282.1	137.1	23.9	5.73
TXDUST01_16*	TXD05H	0.78 (0.12–4.95)	227.4	195.1	49.3	3.96
TXDUST01_17	TXD05H	0.74 (0.12–4.59)	185.7	119.7	29.1	4.12

*INSEKT and DFPC samples were collected. **Based on the dS/dlogD_{ve} fit; Min–Max values are estimated at 0.1 x 10^{-9} m^2 L^{-1}.

Table 4. DFPC-estimated INP concentration for TXD01 and TXD05 samples: H denotes the dry-heated sample. The subscripts of Tot and PM$_1$ represent INP obtained from total aerosol particles and that from PM$_1$ size-segregated aerosol particles, respectively. Standard deviations were derived based on multiple measurements for each sample. Only PM$_{10}$ of TXD01 sample was examined due to the data limitation. This size limit is valid since we observed only < 10 μm aerosol particles in AIDA (**Table 3**). Supermicron INP fraction (%) is calculated by [($n_{INP,total}$ - $n_{INP,PM1}$) / $n_{INP,total}$] x 100.

Dust	n_{INP} x10^3 (L^{-1}) ± standard dev.		Supermicron INP fraction (%)	
	-18°C	-22°C	-18°C	-22°C
TXD01$_{Tot}$	340.0 ± 211.0	2580.0 ± 698.0	**26.5**	**46.5**
TSD01$_{PM1}$	250.0 ± 90.0	1380.0 ± 219.0		
TXD01H$_{Tot}$	1266.7 ± 192.5	7141.7 ± 885.0	**72.4**	**60.2**
TSD01H$_{PM1}$	350.0 ± 120.0	2841.7 ± 375.8		
TXD05$_{Tot}$	770.0 ± 110.0	6780.0 ± 426.0	**58.4**	**48.4**
TSD05$_{PM1}$	320.0 ± 116.0	3500.0 ± 1066.0		
TXD05H$_{Tot}$	508.3 ± 100.0	4575.0 ± 1080.8	**60.7**	**24.6**
TSD05H$_{PM1}$	200.0 ± 45.8	3450.0 ± 715.8		

Table 5. OAF-INP parameterization: List of exponential fit parameters to the $n_{s,geo}(T)$ for T-binned ensemble datasets of lab study as well as field study. The datasets are fitted in the log space. The correlation coefficient, r, for each fit is also shown. All $n_{s,geo}(T)$ values are in m^{-2}. T is in °C. Note the fifth-order polynomial fit function is sensitive for all decimals shown here. To reproduce the fitted curves, we needed to include all decimals.

Fitted dataset: Sample ID (INSEKT sample type)	Fitted T range	Fit Parameters $n_{s,geo}(T) = \exp(a + b\cdot T + c\cdot T^2 + d\cdot T^3 + e\cdot T^4 + f\cdot T^5)$							
		a (m^{-2})	b (m^{-2} °C^{-1})	c (m^{-2} °C^{-2})	d (m^{-2} °C^{-3})	e (m^{-2} °C^{-4})	f (m^{-2} °C^{-5})	r	$\Delta\log(n_{s,geo})/\Delta T$
TXD01 (bulk)	-29°C < T < -7.5°C	-10.419739559253788	-4.736514708000364	-0.19248508975777787	0.0025143767156404874	0.0002817257460974357	3.66476024299544e-06	0.99	0.28
TXD01H (bulk)	-28.5°C < T < -7.5°C	-22.02476692454698	-8.027234773393355	-0.5620907167927012	-0.016652073879196847	-0.00016994936493112665	-1.2200599889511637e-07	0.99	0.26
TXD01 (filter)	-29°C < T < -13.5°C	-649.6092661424044	-166.17848015453706	-16.331424541701384	-0.785403143752226	-0.01845636506788169	-0.00017023048008878034	0.99	0.41
TXD01H (filter, dry-heated)	-28.5°C < T < -12°C	17.885511152572057	-1.8325915290723702	-0.5650878320173172	-0.04817379804678202	-0.0016235221213422987	-1.973016312032128e-05	0.97	0.35
TXD01H (filter, wet-boiled)	-28.5°C < T < -19°C	-28412.092220119186	-6043.63511549024	-511.44780894398167	-21.530974485881597	-0.4508541686398098	-0.003757133824947974	0.99	0.59
TXD05 (bulk)	-28.5°C < T < -10°C	-50.023271755289954	-16.04573078900857	-1.6173561828000045	-0.08074357074021918	-0.0019357893701810924	-1.8076791589170566e-05	0.64	0.35
TXD05H (bulk)	-27°C < T < -9.5°C	-28.41132102063094	-9.820913042395558	-0.9094936795258034	-0.03972654718668897	-0.0007636244274088211	-5.200001963207848e-06	0.99	0.33
TXD05 (filter)	-28.5°C < T < -14°C	-313.3058252180446	-75.912698717769	-6.9043325932941135	-0.30470826275283364	-0.006460682825298372	-5.2755364498764944e-05	0.62	0.42
TXD05H (filter, dry-heated)	-27°C < T < -14°C	-452.01181238097746	-117.32306672273883	-11.762368934161058	-0.5836182871815891	-0.014288215373972207	-0.0001386700575218297	0.97	0.41
TXD05H (filter, wet-boiled)	-27°C < T < -19.5°C	41020.3220707645	9026.327490224949	791.3895483931685	34.55111220994813	0.7512394301270052	0.00650767203399298	0.97	0.61
Field_Median	-25°C < T < -5°C	-29.647010567958052	-16.317058386439328	-2.309495989654582	-0.16257046807120043	-0.005523933523123538	-7.23939690197926e-05	0.94	0.52
Field_Max	-25°C < T < -5°C	-33.22332405003339	-17.91894068815357	-2.537870078194984	-0.17808422538269214	-0.006028509490726683	-7.87080475404568e-05	0.93	0.53
Field_Min	-25°C < T < -5°C	-3.6982332795064234	-5.347998607534987	-0.6782792077804785	-0.04122346827949928	-0.0011424218790211352	-1.193966078225184e-05	0.99	0.44

Table 6. Abundance of major bacterial phyla in dust samples TXD01 and TXD05. Numbers indicate percentage of the OTUs for each phylum in the total bacterial microbiome. The percentage of *Actinobacteria* in the microbiome is increased in aerosolized samples.

Taxonomy	Bulk TXD01	Bulk TXD01 (Dry-Heated)	Aerosolized TXD01	Bulk TXD05	Bulk TXD05 (Dry-Heated)	Aerosolized TXD05
Actinobacteria	40.1%	42.2%	60.1%	51.7%	67.1%	92.9%
Chloroflexi	4.4%	4.9%	4.0%	9.3%	4.0%	1.1%
Unclassified	3.8%	4.0%	4.0%	8.1%	9.9%	2.6%
Proteobacteria	19.9%	16.8%	11.4%	13.0%	10.3%	0.6%
Firmicutes	17.2%	17.5%	13.6%	15.4%	7.3%	2.8%
Bacteroidetes	12.6%	13.1%	6.5%	2.3%	1.4%	0.0%
Gemmatimonadetes	1.6%	1.3%	0.4%	0.1%	0.0%	0.0%
Cyanobacteria	0.2%	0.1%	0.0%	0.0%	0.0%	0.0%
Fibrobacteres	0.1%	0.1%	0.0%	0.0%	0.0%	0.0%
Nitrospinae	0.1%	0.0%	0.0%	0.0%	0.0%	0.0%
Planctomycetes	0.0%	0.0%	0.0%	0.0%	0.0%	0.0%
Rhodothermaeota	0.0%	0.0%	0.0%	0.0%	0.0%	0.0%
Spirochaetes	0.0%	0.0%	0.0%	0.1%	0.0%	0.0%

Table 7. Summary of particle size properties through electron microscopy.

Sample Type	Measured Particles	*Diameter (µm)		**Aspect Ratio	
		Average	Std. Error	Average	Std. Error
TXD01 aerosol	159	0.80	0.03	1.46	0.04
TXD01 residual	185	0.87	0.03	1.56↑	0.04
TXD01H dry-heated aerosol	162	0.82	0.03	1.42	0.03
TXD01H dry-heated residual	126	0.90	0.04	1.48↑	0.05
TXD01 cumulative	632	**0.84**	0.02	1.48	0.02
TXD05 aerosol	194	0.99	0.03	1.37	0.03
TXD05 residual	164	1.17	0.03	1.49↑	0.03
TXD05H dry-heated aerosol	100	1.23	0.04	1.41	0.05
TXD05H dry-heated residual	169	0.90	0.03	1.49↑	0.04
TXD05 cumulative	627	**1.05**	0.02	1.44	0.02

*Average of 2-D cross sections. **Ratio of cross sections (i.e., longer cross section/shorter cross section).

Table 8. Summary of particle composition types through energy dispersive X-ray spectroscopy.

Particle Type	TXD01 Abundance (%)				TXD05 Abundance (%)			
	Aerosol	Residual	Dry-heated Aerosol	Dry-heated Residual	Aerosol	Residual	Dry-heated Aerosol	Dry-heated Residual
Organic	5.0	7.6↑	3.1	9.5↑	8.2	9.1↑	3.0	11.2↑
Salt-rich	34.6	10.3↓	35.8	4.0↓	22.2	4.9↓	15.0	10.1↓
Mineral-rich	57.2	77.8	56.2	70.6	68.0	82.9	79.0	74.6
Other	3.1	4.3	4.9	15.9	1.5	3.0	3.0	4.1